

# Adaptive Segmentation of Knee Radiographs for Selecting the Optimal ROI in Texture Analysis

Neslihan Bayramoglu<sup>1</sup>, Aleksei Tiulpin<sup>1,3</sup>, Jukka Hirvasniemi<sup>2</sup>, Miika T. Nieminen<sup>1,3,4</sup>, and Simo Saarakkala<sup>1,3,4</sup>

<sup>1</sup>Research Unit of Medical Imaging, Physics and Technology (MIPT), University of Oulu, Finland

<sup>2</sup>Department of Radiology and Nuclear Medicine, Erasmus MC, University Medical Center, Rotterdam, The Netherlands

<sup>3</sup>Department of Diagnostic Radiology, Oulu University Hospital, Oulu, Finland

<sup>4</sup>Medical Research Center, University of Oulu and Oulu University Hospital, Oulu, Finland

## ABSTRACT

**Objective:** The purposes of this study were to investigate: 1) the effect of placement of region-of-interest (ROI) for texture analysis of subchondral bone in knee radiographs, and 2) the ability of several texture descriptors to distinguish between the knees with and without radiographic osteoarthritis (OA).

**Design:** Bilateral posterior-anterior knee radiographs were analyzed from the baseline of Osteoarthritis Initiative (OAI) and Multicenter Osteoarthritis Study (MOST) datasets. A fully automatic method to locate the most informative region from subchondral bone using adaptive segmentation was developed. We used an oversegmentation strategy for partitioning knee images into the compact regions that follow natural texture boundaries. Local Binary Patterns (LBP), Fractal Dimension (FD), Haralick features, Shannon entropy, and Histogram of Oriented Gradients (HOG) methods were computed within the standard ROI and within the proposed adaptive ROIs. Subsequently, we built logistic regression models to identify and compare the performances of each texture descriptor and each ROI placement method using 5-fold cross validation setting. Importantly, we also investigated the generalizability of our approach by training the models on OAI and testing them on MOST dataset. We used area under the receiver operating characteristic (ROC) curve (AUC) and average precision (AP) obtained from the precision-recall (PR) curve to compare the results.

**Results:** We found that the adaptive ROI improves the classification performance (OA vs. non-OA) over the commonly-used standard ROI (up to 9% percent increase in AUC). We also observed that, from all texture parameters, LBP yielded the best performance in all settings with the best AUC of 0.840 [0.825, 0.852] and associated AP of 0.804 [0.786, 0.820].

**Conclusion:** Compared to the current state-of-the-art approaches, our results suggest that the proposed adaptive ROI approach in texture analysis of subchondral bone can increase the diagnostic performance for detecting the presence of radiographic OA.

**Keywords—** Osteoarthritis, bone texture analysis, adaptive region of interest, knee, radiograph

## 1 Introduction

Along with the progression of osteoarthritis (OA), subchondral bone (SB) is subject to changes in its structure and composition<sup>1,2</sup>. In knee radiography, a strong association between SB texture and severity of OA has been reported<sup>1,3–14</sup>. In particular, the thickness of subchondral cortical plate is increased especially in the medial compartment knee OA<sup>1</sup>. Moreover, ladder-like appearance is observed in horizontal trabeculae in OA<sup>1</sup>. Although the thickness and volume of subchondral bone increases in OA, it is weaker and less mineralized than normal bone<sup>1</sup>. It is also known that trabecular network adapts to alterations in joint loading relatively quickly<sup>15</sup>.

Plain radiography (X-ray imaging) is a cheap and widely available clinical modality to detect the presence and severity of OA<sup>16</sup>. Unfortunately, plain radiography has generally relatively low sensitivity for detecting early osteoarthritic changes<sup>17</sup>. Further, the status of SB is rarely assessed from plain radiographs in clinical practice, and instead, the overall severity of OA within a joint is visually evaluated or semi-quantitatively graded. However, it has been proposed that the quantification of SB structural changes with texture analysis from radiographs can lead to development of more sensitive OA biomarkers<sup>9,15</sup>.

Various studies have focused on quantitative analysis of knee joint radiographs<sup>11,16,18–21</sup>, and in particular on SB texture

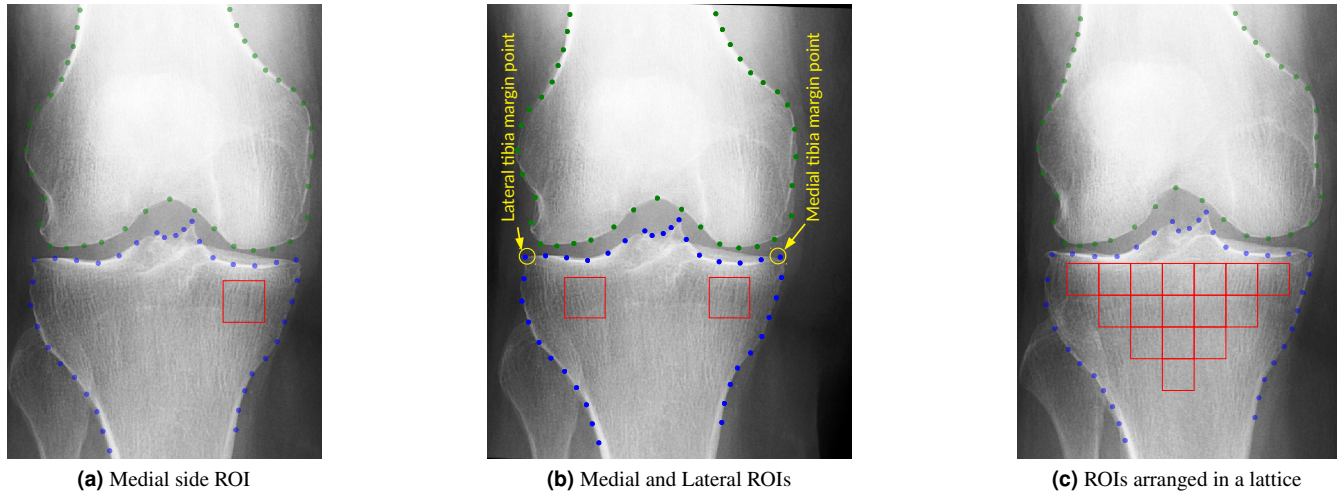


**Figure 1.** Examples of region-of-interest (ROI) placement for texture analysis in previous studies. Here, a) shows an example of medial side ROI, b) shows medial and lateral ROIs together with medial and lateral tibia margins, and c) square ROIs arranged in a lattice. Typical landmark points are also marked in the images.

analysis<sup>8,9,22–25</sup>. Changes in SB texture in the radiograph have been quantified based on roughness, anisotropy, and orientation of texture elements mostly by fractal methods<sup>1,3–14,26,27</sup>. Only a few studies have investigated non-fractal methods for classifying SB texture<sup>9,11,23,28–30</sup>. The potential advantage of using non-fractal methods is to capture statistical characteristics of textures and added discriminative power by distinguish key texture primitives such as edges, corners and uniform regions<sup>31</sup>. The placement of region-of-interest (ROI) is a crucial step in bone texture analysis. Most often it is done manually<sup>9,14,32–34</sup>, but there exist some studies where semi-automatic<sup>4,29</sup> and fully automatic approaches<sup>11,35</sup> have been used for the ROI placement. It is well known that bony changes in OA are typically not uniform throughout the subchondral bone, but instead highly localized regional differences in bone microstructure can be observed<sup>2</sup>. Consequently, placement of ROI could have a significant effect on the image analysis results, and thus, selecting ROI for texture analysis plays an important role to accurately quantify changes in subchondral bone structure.

Earlier studies have used predefined rectangular ROIs either at a single location or at multiple sites<sup>1,6,9,14,27,29,33,35</sup> (see Figure 1). In particular, rectangular ROIs are often placed immediately beneath the inferior border of the medial or lateral cortical plates<sup>3,5,9,13,14,35,36</sup>. Most of the approaches found in the literature employ medial ROI as medial OA has a much higher prevalence in the population. Previously, the outer regions of the tibial compartment have been excluded from the analysis intentionally to avoid the inclusion of periarticular osteopenia adjacent to marginal osteophytes<sup>13</sup>. However, only a few studies have questioned the effects of the placement, size, and shape of ROI on the prediction of knee OA in texture based methods<sup>27,29</sup>. Specifically, Janvier et al.<sup>27</sup> demonstrated the importance of the ROI placement by arranging square ROIs in a lattice using fractal descriptors (See Figure 1). In their study, the square side length was equal to  $1/7$  of the tibial width minus an offset of 10% to prevent the periarticular malformations. They concluded that the success of predicting incident OA depends on the location of the ROI.

In this study, we propose a fully automated method to locate the most informative subchondral bone ROI in plain radiographs using adaptive segmentation. We conducted extensive analyses on the placement of texture ROI for both femur and tibia, including their outer regions, and comparing the results using several texture descriptors using cross-validation and an independent test set. The flowchart of the proposed pipeline is illustrated in Figure 2. The method is based on oversegmentation and it partitions the knee images into compact regions that respect the local texture boundaries. We believe that such division is more natural than employing fixed rectangular ROIs because texture boundaries do not follow straight lines, but are instead following true anatomical structure of the bone.

## 2 Materials and Methods

### 2.1 Data

We used the data from the Osteoarthritis Initiative (OAI) and Multicenter Osteoarthritis Study (MOST). OAI comprises individuals at risk of development of symptomatic femorotibial OA. A total of 4,796 men and women at ages 45–79 were enrolled to the study between 2004 and 2006. Images were graded by Kellgren–Lawrence (KL) scoring system. We selected all

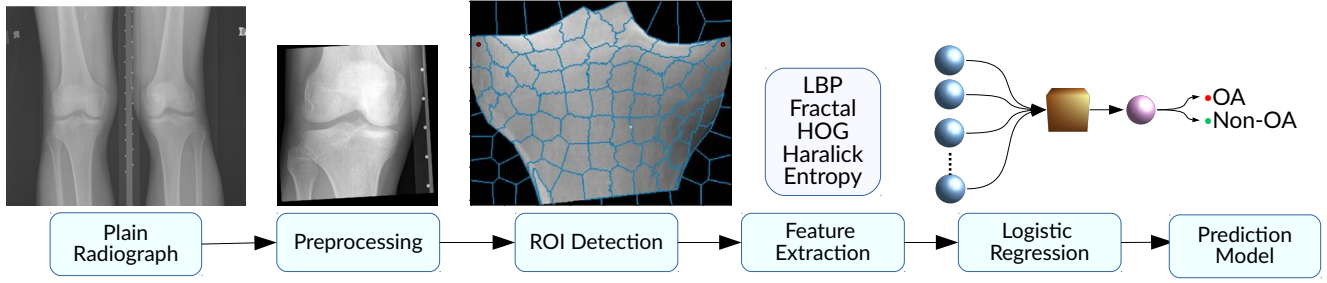


**Figure 2.** Flowchart of our classification pipeline for the detection of radiographic OA. As a first step, we localized bone landmarks using BoneFinder software (see Materials and Methods for more details). Subsequently, we applied global contrast normalisation and histogram truncation between the 5<sup>th</sup> and 99<sup>th</sup> percentiles. We then normalised the data to have a 0.2mm pixel spacing. Finally, each knee is rotated in order to have an aligned horizontal tibial plateau. After ROI detection and texture description, we applied logistic regression in a 5-fold cross validation setting to measure the performance of all the methods.

the knees at baseline that were graded by KL score on both knees thereby excluding the cases with total knee replacement. Multicenter Osteoarthritis Study (MOST) comprises 3,026 individuals aged 50–79 years who either had radiographic knee OA or were at high risk for developing the disease. At the baseline clinical visit, all the subjects underwent weight-bearing posteroanterior fixed flexion knee radiographs. From MOST data, we selected all the subjects at baseline with posteroanterior view having acquired with 10 degrees beam angle (PA10) of the knee given that both joints are graded with KL score. Knees with total knee replacement were excluded. The details about OAI and MOST datasets used in this study are presented in Table 1. Future details about OAI and MOST can be found on <http://www.oai.ucsf.edu/> and <http://most.ucsf.edu>, respectively.

In our analysis, we trained algorithms on OAI dataset and tested them on MOST data which are independent study materials. Such a validation is very important to assess the methods' performance objectively and its ability to analyze unseen data.

**Table 1.** Description of the data. We used the data from the OAI dataset and MOST dataset at baseline with posteroanterior view acquired with 10 degrees beam angle (PA10) of the knee given that both joints are graded with KL score. Knees with total knee replacement were excluded. Subject wise partitioning was used to split data into train and test sets in a 5-fold cross validation setting.

	OAI	MOST
Number of knees	9012	3644
Number of subjects	4506	1822
Number of samples where $KL < 2$	5045	2247
Number of samples where $KL \geq 2$	3967	1397

## 2.2 Data Preprocessing

We extracted anatomical landmark points (keypoints) of knee image using BoneFinder<sup>®37</sup> tool. In the preprocessing pipeline, the 16-bit DICOM images are first normalized using global contrast normalisation and a histogram truncation between the 5<sup>th</sup> and 99<sup>th</sup> percentiles. These images were eventually converted to 8-bit images (0 – 255 grayscale range). The image resolution which was not standardized in the database was also standardized to 0.2 mm using a bicubic interpolation. Finally, using landmark points, each knee was rotated to horizontally align the tibial plateau.

## 2.3 Adaptive Region of Interest

This section describes our developed adaptive region segmentation and ROI selection approach. Firstly, we segmented tibia and femur from the background using the landmark points. Secondly, we performed oversegmentation of the bone region into subregions separately for femur and tibia using superpixel labelling<sup>38</sup> (Figure 4). Superpixel labelling is an oversegmentation strategy for partitioning images into smaller patches that are spatially contiguous and similar in intensity. Superpixel clusters produce compact regions (subregions, superpixels) that follow image boundaries.

To generate the superpixels we used Simple Linear Iterative Clustering (SLIC) because of its simplicity and flexibility in the compactness and number of the superpixels it generates<sup>38</sup>. The algorithm adopts *k-means* clustering in intensity and spatial domain. Starting from *k* regularly spaced cluster centers, each pixel in the image is associated with the nearest cluster center.

The process of associating pixels with the nearest cluster center and recomputing the cluster center is repeated iteratively until convergence. At each iteration, superpixels are reassigned to the average color and position of the associated input pixels.

The distance measure ( $D$ ) in computing the similarity between the pixel and the cluster center is an Euclidean norm in the five-dimensional space (color (CIELAB) + spatial):

$$D = \sqrt{d_c^2 + \frac{d_s^2}{S} m^2}, \quad (1)$$

where  $d_c$  is the color distance,  $d_s$  is the spatial distance,  $m$  is a parameter that weighs the relative importance between the color similarity and the spatial proximity, and  $S$  is a parameter indicating the size of the superpixels. Compactness,  $C$ , (i.e. more compact superpixels have lower area to perimeter ratio) can be then controlled by  $m$ . The ability to specify the amount of superpixels and the ability to control the compactness are important properties of this method. In addition, SLIC exhibit state-of-the-art adherence to image boundaries.

### **Detection of the Most Informative Region**

In the following step, we used  $M$  regularly placed grid points,  $g_i, i \in 1, 2, \dots, M$ , in order to select approximately the same subregion for all subjects (Figure 4a) for feature extraction and machine learning stages. Grid points do not necessarily end up in different regions. We intentionally placed relatively dense grid compared to the average size of superpixels to cover the full bone region. Therefore, multiple points may fall in the same subregion (superpixel) but this does not hamper the analysis. Each subregion  $r_i$  is then described by a feature vector  $f\{r_i\}$ . Finally, we evaluated and compared  $M$  regions based on textural properties. In this step, we employed Local Binary Patterns (LBP) descriptor to detect the most informative (optimal) region. Here, we defined the most informative region as the subregion where the texture classifier (based on LBP features) performs best to distinguish OA samples from non-OA. Figure 3 shows the first two informative regions on tibia and femur based on grid locations. We provided the full analysis in the material. Instead of utilizing grid based locations, we made a second pass to detect the adaptive regions that correspond to explicit pixel locations which fall (2mm, 2mm) inside the medial tibia margin point and the lateral tibia margin point and utilized them in the rest of the experiments. Heat-map representations of these regions were obtained by averaging the corresponding subregions over all subjects in the database (average mask). The results suggest that outer medial tibia side provides richer information than other regions from the point of texture analysis.

Figure 4b shows the process of averaging and also individual masks that correspond to the outermost medial region which is denoted by t26 (tibia region 26) that follows the lattice numbering. The average mask for the most informative region shows that there is a large portion of overlap between the segmentation masks. We take the advantage of this finding to reduce the computational complexity of the overall method in the following experiments. Instead of segmenting the tibia of each individual subject, we employed the mask which was obtained by thresholding the average mask using Otsu's method. Thresholded mask and its contour on a sample image are presented in Figure 4c.

## **2.4 Standard ROI**

We utilized the extracted landmark points to locate standard rectangular ROI in a fixed region on each knee. We followed the literature<sup>3,5,11,36,39</sup> to locate 'standard' ROI: We used a square patch placed immediately beneath the tibial plateau with dimensions proportional to the width of the knee in the centre of the medial condyle of tibia (see Figure 5) .

## **2.5 Analysis of Texture Features**

### **Texture Descriptors**

Although texture descriptors have been applied to plain knee radiographs for years, Fractal Signature Analysis (FSA) or fractal dimension (FD) and its variations remain the main method to analyse OA texture until today<sup>1,3-14,26,27</sup> since 1990's. Other texture descriptors used in OA analysis include simple pixel features<sup>11</sup>, Haralick's texture features based on the Gray Level Co-occurrence Matrix (GLCM)<sup>28</sup>, Gabor filter banks<sup>30</sup>, Entropy<sup>29</sup>, Wavelet Transform<sup>23</sup>, Tamura texture features<sup>28</sup>, and Local Binary Patterns (LBP)<sup>9</sup>. Sometimes the combination of different texture descriptors and also shape descriptors have been used<sup>11,28,40</sup>.

Fractals, which is a measure of surface 'roughness', have been used to analyze and quantify very complex shapes or structures. FD is calculated by taking the pixel intensity differences at varying scales of the image. Then the slope of the line which is fitted to a log-log plot of the intensities across the scales, determines the FD. In OA related studies, it was first used by Lynch et al.<sup>3</sup> to quantify trabecular bone texture. The FD was linked to spacing, variation in thickness and orientation, and cross-connectivity of the trabeculae structure<sup>14</sup>. However, FSA is sensitive to image artifacts and noise<sup>41</sup>.

As noted earlier, a variety of methods for FD calculation has been proposed in the literature (power spectrum method, maximum likelihood method, tile counting method, box counting method, blanket methods, modified Hurst orientation



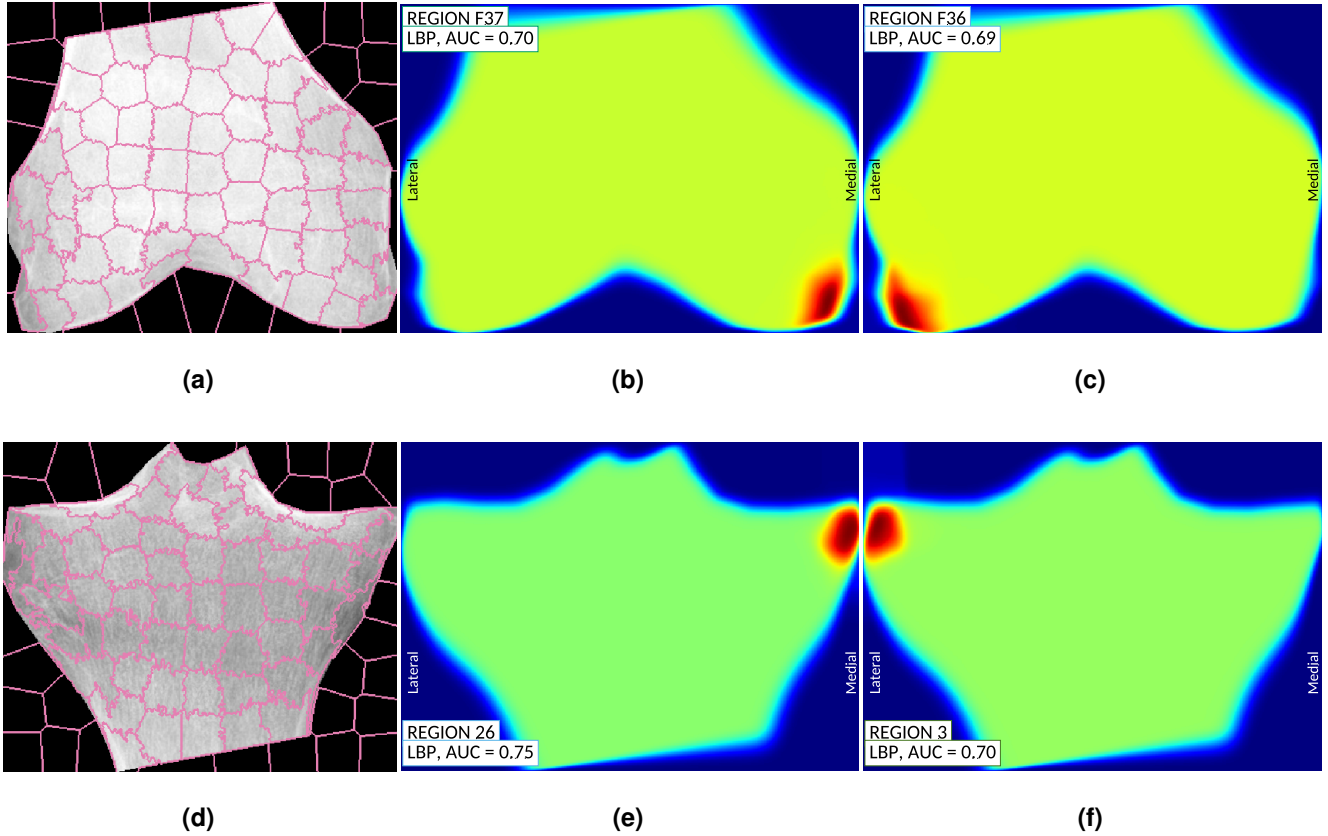
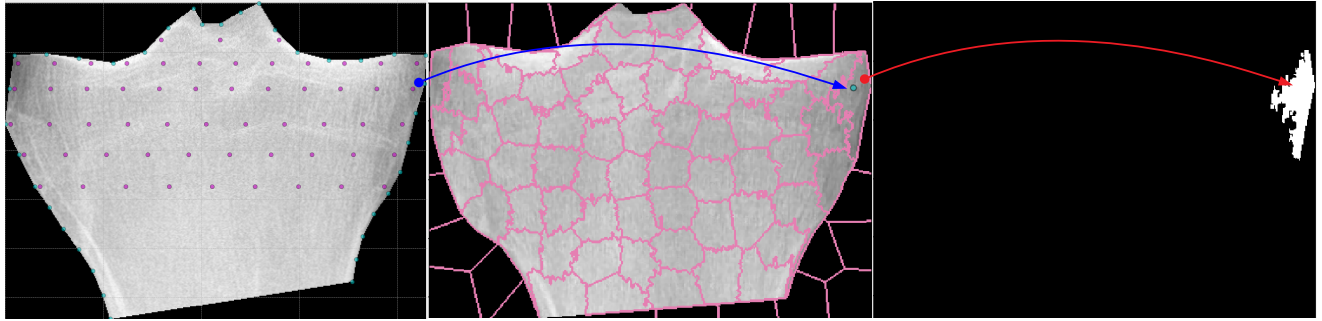
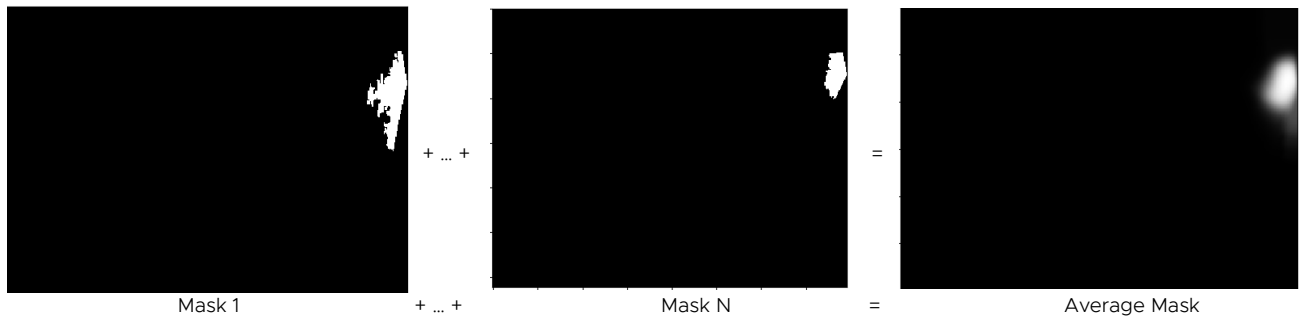


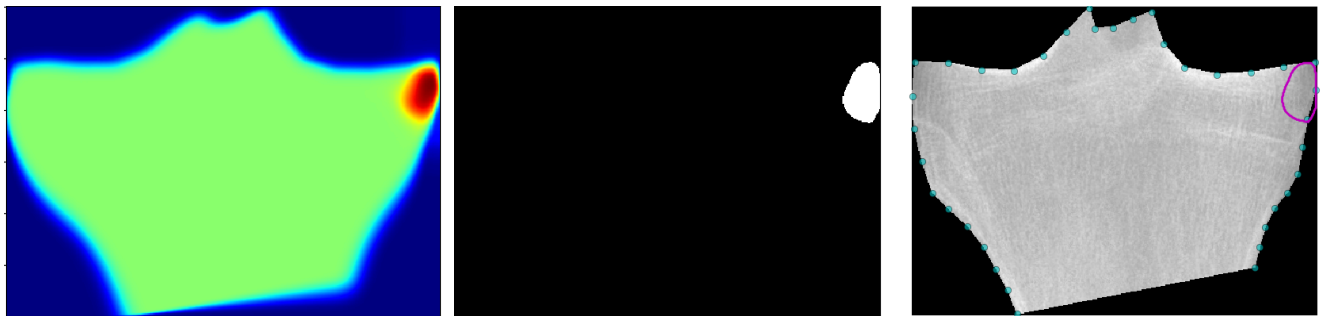
**Figure 3.** The most informative regions we found are located at the sites where osteophytes are typically occurring. The subfigure, (a) demonstrates a sample showing the superpixel segmentation boundaries of a femur image, (b) shows the most informative region of femur **f37** which is located at medial margin, and (c) shows the second most informative region of femur **f36** which is located at lateral margin, (d) Demonstrates a sample showing the superpixel segmentation boundaries of a tibia image, (e) shows the most informative region of tibia **t26** which is located at medial margin and (f) shows the second most informative region of tibia which is **t3** located at lateral margin based on our grid placement.



**(a)** Presentation of our adaptive region segmentation and region of interest selection approach. We first placed a dense grid (57 points) on each subject proportional to its size. Subsequently, for each grid point (location), in order to assess its descriptive power we used the segmented region that encloses the grid point. Segmented region was then described by LBP and the corresponding vector was fed into the machine learning pipeline (see Figure 2). Similar analysis was also done for femur compartment.



**(b)** In order to obtain the mean shape and the location of most informative region, masks of the adaptive regions that corresponds to the same location were accumulated over all subjects.



**(c)** (Left to right) Average mask obtained from region  $\pm 2\sigma$  overlaid on average tibia image. Thresholded mask using Otsu's method (adaptive mask ROI). Boundaries of the adaptive mask ROI is shown on a sample tibia image.

**Figure 4.** Overview of the developed adaptive region segmentation and the region-of-interest (ROI) selection approach.

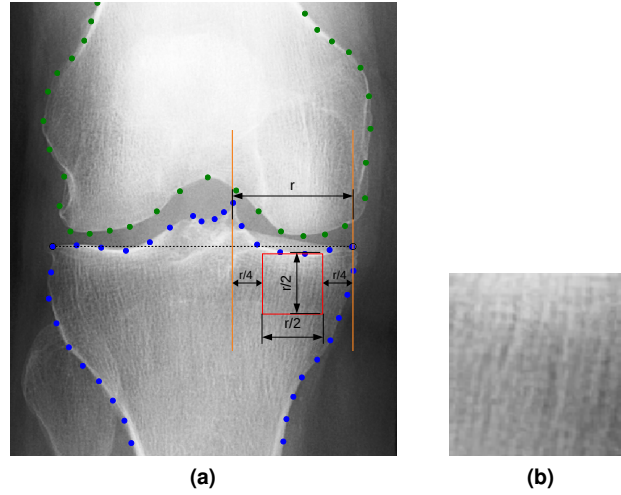


**Figure 5.** Illustration of (a) the placement of standard region of interest (ROI) and (b) corresponding (cropped) ROI image.

transform, variance orientation transform, augmented variance orientated transform). Differences in the techniques for measuring FD result different numerical values, albeit they aim at estimating surface roughness. Although they are correlated, they do not directly measure the same image property. Therefore, it is not easy to reproduce and compare fractal based approaches. In addition, the narrow range of the FD measurement values susceptible to limited discrimination power.

GLCM represents the distance and angular spatial relationship of pixels which is then used to derive several statistics. Haralick proposed a set of fourteen feature measures based on GLCM including contrast, correlation, entropy, variance, sum average, sum variance, sum entropy, angular second moment, difference variance, difference entropy, information measure of correlation 1, information measure of correlation 2, and inverse difference moment. The well-known local binary descriptor “Local Binary Patterns” labels image pixels by thresholding the neighbourhood of each pixel with the center value and considering the result as a binary number<sup>42</sup>. Then distribution of LBP code of an image is used to describe the texture by a histogram vector. Shannon entropy which measures the amount of randomness of gray levels is also used to characterize the texture of an input image. Histogram of Oriented gradients (HOG)<sup>43</sup> employs distribution of the directions of the image gradients. Image is divided into a overlapping rectangular grid of cells grouped into  $k \times k$  blocks. A histogram of the gradient directions is then computed within each cell of each block.

### Implementation Details

After preprocessing the raw radiography data, we select ROI for computing the texture descriptors. We utilized both classical approach (rectangular ROI) and adaptive ROI in our experiments. We evaluated and compared FD, LBP, Haralick features, Shannon entropy, and HOG.

For FD computation, we used the implementation from<sup>44</sup> which calculates FD separately for vertical and horizontal trabecular structures within the ROI. Compared to<sup>44</sup>, we increased the maximum size of the flat disk from 2mm to 3.2mm which is used as a structuring element for calculating the FD. We also noticed that the size of the structuring element affects the performance of the method such that bigger structuring element results slightly better. We utilized only the first 13 features from Haralick descriptor using publicly available open source Mahotas library<sup>45</sup>. For other descriptors and SLIC, we used scikit-learn<sup>46</sup> python package which is also an open source library. For all experiments, we chose empirically the compactness parameter as 0.08 and the number of regions as 100 for the initial region segmentation (i.e. SLIC parameters). The best parameters for standard ROI for LBP and HOG were determined by grid search technique in scikit-learn<sup>46</sup> package. In order to favor the standard ROI, the optimal parameters on standard ROI were employed in adaptive ROI experiments. Search space of parameters and the best values that optimized the AUC value on cross-validation are given in material in Table S1.

## 2.6 Statistical Analysis

In order to assess how the results of our analysis generalize over a set of independent data we used i) cross-validation and ii) validated our trained model with an independent test set that is completely different from the training one. Cross-validation is a method for estimating predictive performance and also for model selection. For large sample sizes, the K-fold cross-validation method gives nearly unbiased estimator. In K-fold cross-validation, the training data is divided into  $K$  disjointed parts of approximately equal size. Then the learning algorithm is trained on  $K - 1$  of  $K$  independent subsets (training set) and the remaining one (test set) is used to estimate the predictive performance (expected loss on unseen future samples). The algorithm

**Table 2.** Comparison of texture descriptors on OAI calculated from Standard ROI vs Adaptive ROI. Scores are given by ROC AUC and Precision-Recall AP with 95% confidence interval in parentheses on a 5-fold cross validation setting.

OAI - Exp 1			
Method	Score	Standard ROI	Adaptive mask $\tau 26$
LBP	AUC	0.685 [0.674, 0.696]	<b>0.761 [0.751, 0.771]</b>
	AP	0.653 [0.639, 0.665]	<b>0.737 [0.724, 0.749]</b>
Fractal	AUC	0.621 [0.609, 0.633]	<b>0.664 [0.652, 0.675]</b>
	AP	0.570 [0.556, 0.584]	<b>0.611 [0.597, 0.624]</b>
HOG	AUC	0.651 [0.640, 0.662]	<b>0.742 [0.731, 0.752]</b>
	AP	0.603 [0.590, 0.616]	<b>0.708 [0.695, 0.720]</b>
Haralick	AUC	0.618 [0.607, 0.629]	<b>0.667 [0.655, 0.678]</b>
	AP	0.573 [0.560, 0.585]	<b>0.634 [0.620, 0.647]</b>
Entropy	AUC	0.585 [0.573, 0.596]	<b>0.587 [0.574, 0.598]</b>
	AP	<b>0.543 [0.529, 0.555]</b>	0.530 [0.517, 0.543]

**Table 3.** Comparison of texture descriptors on MOST calculated from Standard ROI vs Adaptive ROI. Scores are given by ROC AUC and Precision-Recall AP with 95% confidence interval in parentheses on a 5-fold cross validation setting.

MOST - Exp 2			
Method	Score	Standard ROI	Adaptive mask $\tau 26$
LBP	AUC	0.778 [0.760, 0.792]	<b>0.797 [0.781, 0.812]</b>
	AP	0.733 [0.712, 0.751]	<b>0.754 [0.735, 0.772]</b>
Fractal	AUC	0.704 [0.685, 0.720]	<b>0.729 [0.711, 0.745]</b>
	AP	0.600 [0.576, 0.624]	<b>0.652 [0.628, 0.673]</b>
HOG	AUC	0.738 [0.721, 0.754]	<b>0.790 [0.774, 0.804]</b>
	AP	0.682 [0.659, 0.702]	<b>0.704 [0.678, 0.725]</b>
Haralick	AUC	0.701 [0.682, 0.717]	<b>0.791 [0.774, 0.806]</b>
	AP	0.589 [0.565, 0.612]	<b>0.744 [0.724, 0.763]</b>
Entropy	AUC	<b>0.672 [0.653, 0.688]</b>	0.610 [0.591, 0.628]
	AP	<b>0.569 [0.545, 0.591]</b>	0.516 [0.493, 0.537]

is trained  $K$  times, each time using a different test partition. The estimate of error rate is the average of the errors incurred on all folds. Here we evaluate subject-wise cross-validation which is more reliable than record-wise cross-validation to assess the prediction accuracy of a machine learning algorithm. The error rate measures how well the two classes in the data set are separated. We present the area under the receiver operating characteristic curves (ROC AUC) which is also called  $c - index$ , a common metric to measure classifier performance effectively. ROC AUC provides is a combined measure of sensitivity and specificity. The higher the AUC, the better the predictive performance of the classification method. In addition, we present average precision score which quantifies precision-recall curves similar to AUC. The implementation is done using scikit-learn<sup>46</sup> package.

We used two-class regularized logistic regression (LR) to predict the image level label (OA vs non-OA). To mitigate overfitting, we employed regularization. Features obtained by texture descriptors were properly standardized using mean and variance of the training data of each fold.

### 3 Results

We compared the performance of texture descriptors on the standard ROI and on the best adaptive mask ROI ( $\tau 26$ ). Tables 2,3, and 4 show the performance of Logistic Regression classification for five different texture descriptors with different test and training data.

#### Cross Validation

In Table 2, we present the ROC AUC and PR AP values for OAI dataset where we used 5-fold cross validation. From this table, it can be seen that the performance of the classifier increases when the texture descriptors are calculated from adaptive ROI instead of standard ROI. The highest differences were observed with LBP (AUC 7.6%) and HOG (AUC 9.1%) descriptors. We

**Table 4.** Comparison of texture descriptors, on an independent test set (MOST) where training data is OAI, calculated from Standard ROI vs Adaptive ROI. Scores are given by ROC AUC and Precision-Recall AP with 95% confidence interval in parentheses on a 5-fold cross validation setting.

Method	Score	Train: OAI, Test: MOST - Exp 3	
		Standard ROI	Adaptive mask $\tau 26$
LBP	AUC	0.778 [0.761, 0.794]	<b>0.818 [0.802, 0.832]</b>
	AP	0.717 [0.694, 0.737]	<b>0.779 [0.760, 0.795]</b>
Fractal	AUC	<b>0.699 [0.680, 0.715]</b>	0.682 [0.663, 0.699]
	AP	<b>0.602 [0.577, 0.624]</b>	0.582 [0.558, 0.606]
HOG	AUC	0.718 [0.700, 0.734]	<b>0.800 [0.785, 0.813]</b>
	AP	0.640 [0.617, 0.661]	<b>0.725 [0.703, 0.746]</b>
Haralick	AUC	0.683 [0.664, 0.700]	<b>0.762 [0.745, 0.777]</b>
	AP	0.585 [0.561, 0.607]	<b>0.711 [0.689, 0.729]</b>
Entropy	AUC	<b>0.673 [0.654, 0.690]</b>	0.611 [0.591, 0.630]
	AP	<b>0.571 [0.547, 0.593]</b>	0.517 [0.493, 0.538]

made a similar analysis for MOST dataset and presented the results in Table 3. Consistent with previous finding, both ROC AUC and PR AP scores for adaptive ROI are better except Entropy descriptor. Figure 6 shows the ROC and PR curves for OAI data. The ROC and PR curves for MOST data are presented in Figure S2. In addition, we demonstrated the effect of region selection (standard ROI vs. adaptive mask ROI) with ROC and PR curves. Figure 7 demonstrates the ROC and PR curves for LBP, fractal dimension, and entropy descriptors for OAI dataset.

#### Independent Test Set

In Table 4, we presented the results where we used the OAI data for training and the MOST data for testing (validation experiment). We also see from this table that utilizing adaptive mask ( $\tau 26$ ) clearly improves the classification performance over standard ROI for LBP, HOG, and Haralick descriptors where they provide higher classification rate compared to Fractal dimension and Entropy. We also show the ROC and PR curves for the validation experiments in Figure S3.

#### Feature and Region Combination

We analyzed the effect of feature combination on tibial medial margin and also analyzed the region combination (combining features from medial margin and lateral margin) on the classification performance. Table S2 shows ROC AUC and AP values for feature combination on region  $\tau 26$ . Combination of LBP with HOG, FD, and Haralick yielded AUC of 0.774 [0.764, 0.783] and AP of 0.754 [0.742, 0.765] on OAI which is only slightly higher than LBP alone. Similarly, for MOST, we found that feature combination of LBP and HOG which yielded the best performance with AUC of 0.808 [0.793, 0.822] and AP of 0.766 [0.747, 0.782] did not provide significant performance difference in AUC and in AP when compared to LBP alone. In Table S3, we presented classification performances for combining features from multiple ROIs from lateral and medial side of tibia (e.g.  $LBP_{26} + LBP_3$ ). Combination of LBP features from lateral and medial tibia margins yielded AUC of 0.791 [0.782, 0.801] and AP of 0.778 [0.767, 0.788] on OAI. We observed similar performance increase with other descriptors (around AUC of 2%) when combined from lateral and medial tibia regions for OAI and MOST as well.

## 4 Discussion

In this paper, we investigated the placement of ROI for SB texture analysis of knee radiographs. Using automatic oversegmentation method, we found that the most informative bone region associated in OA was located at the tibial margin in the medial side of the knee. We observed that this ROI has a profound effect on bone texture analysis, and this could be due to absorption of uneven mechanical load across the joint<sup>47</sup> and osteophytes that form along joint margins.

The framework presented in this study demonstrated that the performance of the current state-of-the-art approaches used for texture analysis could significantly be improved using the proposed adaptive ROI approach. However, results regarding the entropy and FD are mixed. This could be explained by the higher sensitivity of entropy and FD to the noise and image size<sup>41,48</sup>.

We observed that LBP yielded the best performance in all experimental settings with AUC of 0.761 [0.751, 0.771] and AP of 0.737 [0.724, 0.749] on OAI, AUC of 0.797 [0.781, 0.812] and AP of 0.754 [0.735, 0.772] on MOST, and AUC of 0.818 [0.802, 0.832] and AP of 0.779 [0.760, 0.795] on validation setting when evaluated on adaptive mask ROI ( $\tau 26$ ). HOG showed the second best performance and yielded slightly lower AUC and AP compared to LBP. We obtained similar classification performances with FD and Haralick features. We also observed that entropy lacks discriminative power in classification of



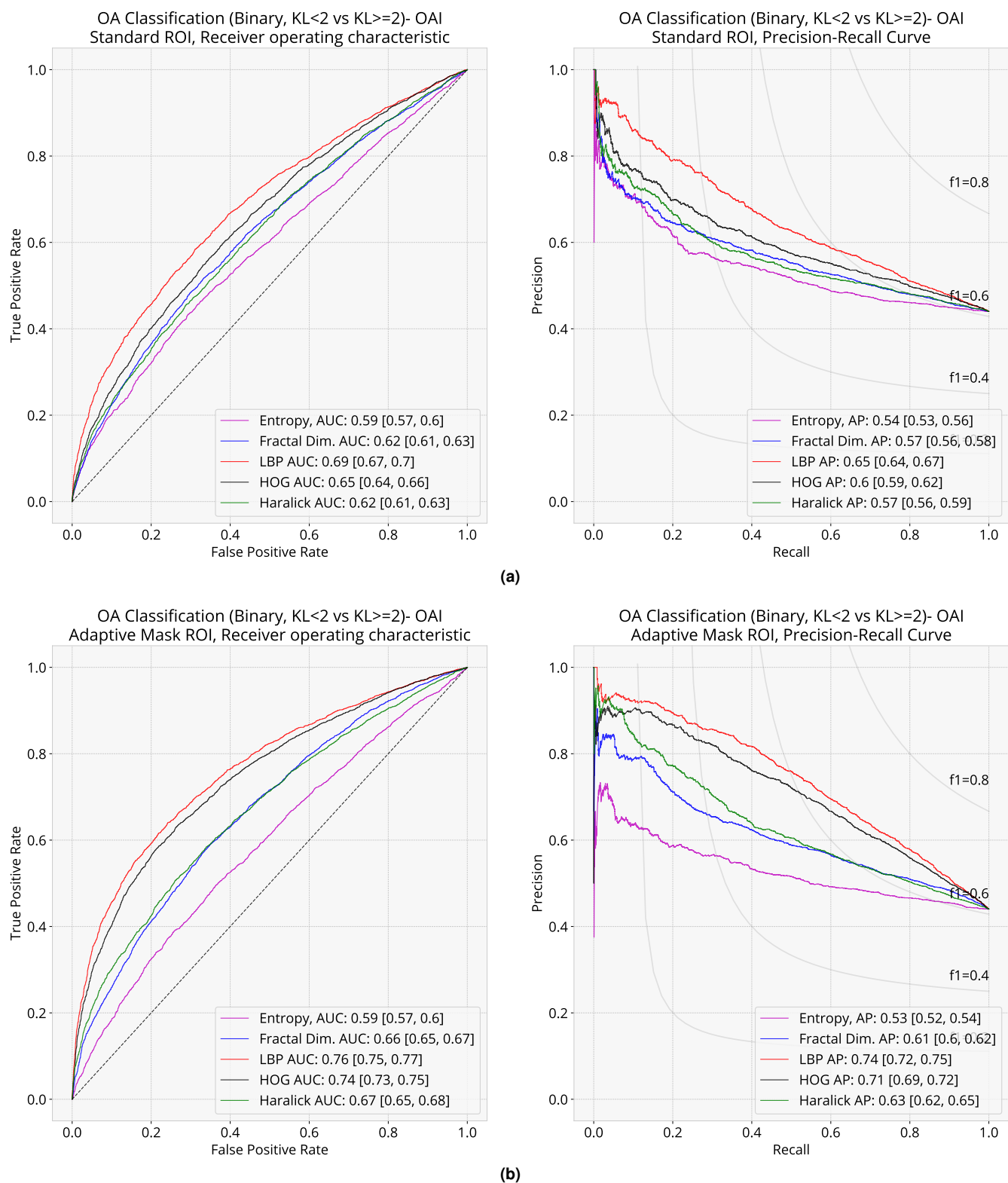
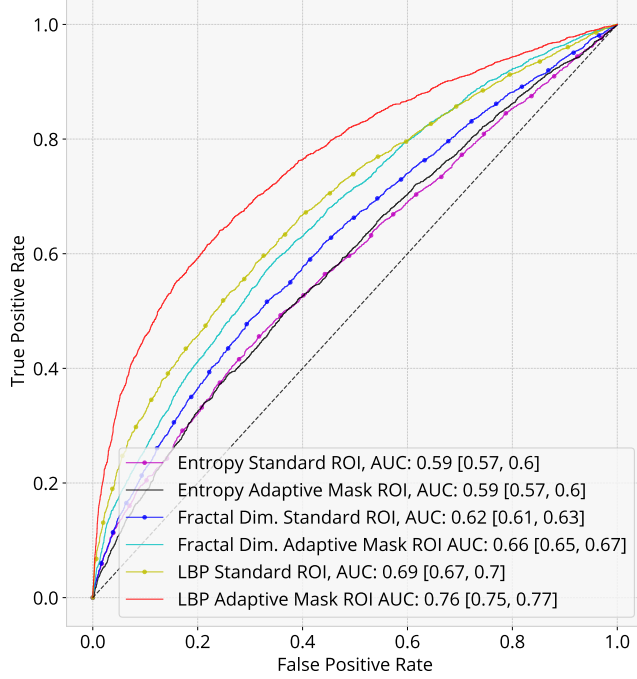
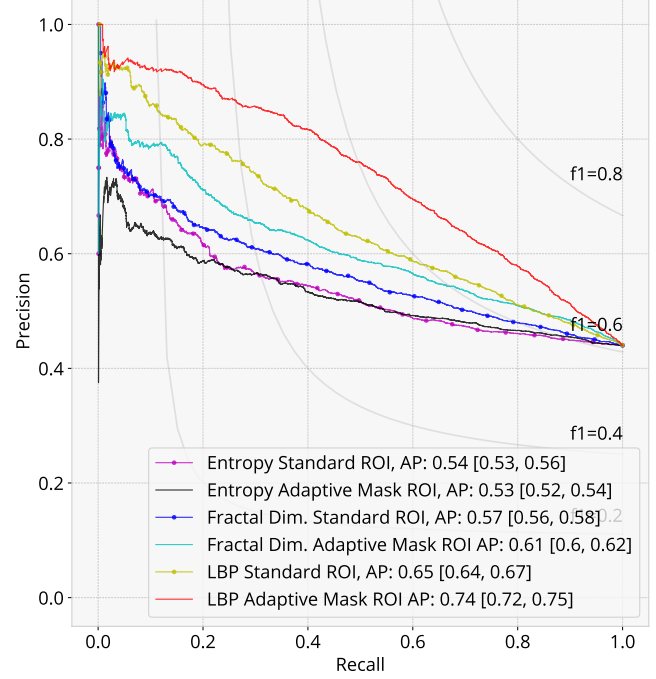


**Figure 6.** Classification performance of texture descriptors with (a) standard ROI and (b) adaptive mask ROI on OAI with logistic regression on 5-fold cross validation setting. In ROC plots, labels show AUC values and labels in PR curves show AP values with 95% confidence intervals in parentheses.

OA Classification (Binary,  $KL < 2$  vs  $KL \geq 2$ )- OAI  
Standard vs. Adaptive Mask ROI, Receiver operating characteristic

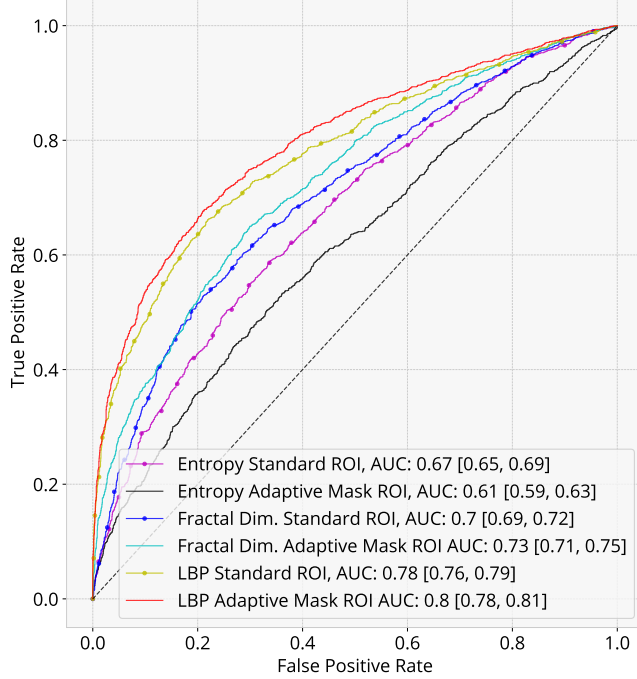


OA Classification (Binary,  $KL < 2$  vs  $KL \geq 2$ )- OAI  
Standard vs. Adaptive Mask ROI, Precision-Recall Curve

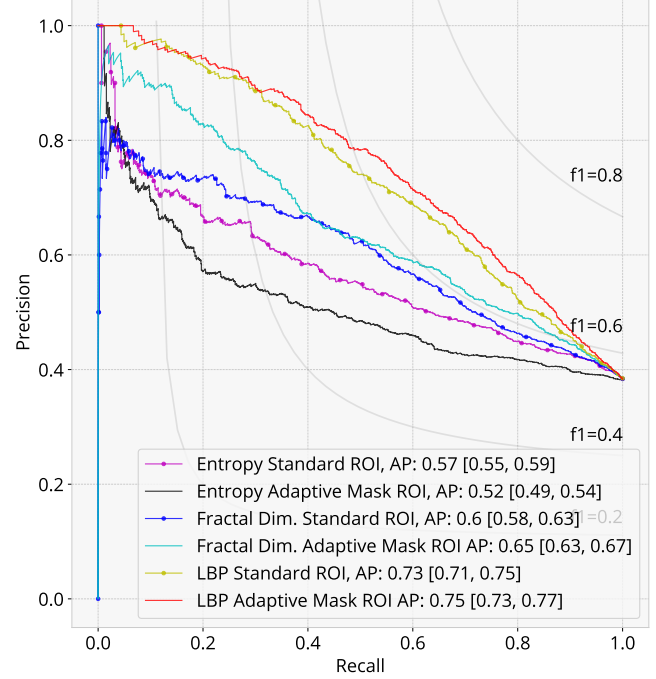


(a)

OA Classification (Binary,  $KL < 2$  vs  $KL \geq 2$ )- MOST  
Standard vs. Adaptive Mask ROI, Receiver operating characteristic



OA Classification (Binary,  $KL < 2$  vs  $KL \geq 2$ )- MOST  
Standard vs. Adaptive Mask ROI, Precision-Recall Curve



(b)

**Figure 7.** Comparison of standard ROI vs adaptive mask ROI with (a) OAI and (b) MOST using logistic regression on 5-fold cross validation setting. In ROC plots, labels show AUC values and labels in PR curves show AP values with 95% confidence intervals in parentheses.

bone texture patches. Although both entropy and FD are widely adopted texture descriptors in OA research<sup>1,3–14,26,27,29</sup>, they performed significantly poorer than LBP in our experiments.

When we used the test data (MOST) which is independent from the training data (OAI) in our validation experiments (Exp 3), we observed that classification performance was not affected, even slight improvements were obtained with LBP and HOG descriptors. This may be explained by different distribution and amount of training samples (2915 vs 9012), and, potentially, imperfect annotations of KL grades<sup>16,49</sup>.

Combination of different texture features (e.g. HOG and LBP) did not provide a significant performance improvement over a single descriptor. For some cases, the classification performance even decreased, which can be explained by multicollinearity, i.e., several individual texture features are strongly inter-correlated leading to numerically unstable regression models. On the other hand, when we concatenated a particular texture descriptor from medial and lateral side, the classification performance improved (Table S3). This is an indication that lateral and medial margin may provide complementary information regarding the bone textural changes in OA.

We observed that, in OA, the radiographically most distinctive bony changes occur at the medial tibia margin, and all the compartments including subchondral cortical plate and subchondral trabecular bone are affected. The alignment of the adaptive region could be correlated with the uneven force that tibia experiences in OA<sup>47</sup>. It could also follow the knee alignment due to deformity. Therefore, it would be interesting to investigate the associations between adaptive ROI alignment and mechanical/anatomic axis angle.

In the light of the experimental results, we believe that the performance of texture analysis to quantify bony changes in radiographic OA could be improved using more robust texture descriptors than the most popular FD. The experimental results of the texture descriptors like LBP and HOG for detecting the radiographic OA presence are convincing, and these approaches are not that sensitive for changes in radiographic acquisition protocols<sup>4</sup>. Thus, they could be applied in clinical decision support tools in the future. In addition to better texture descriptors, the predictive ability of such automated tools could benefit from inclusion of other image features, such as joint shape, osteophytes and joint space width.

Although we have presented a novel method to localize the optimal ROI to improve the performance of the texture analysis, this study has still some limitations. First, the general limitation in application of the machine learning methods to a clinical setting is generalizability of the model due to potential bias associated with the training data and inherited bias due to algorithms. However, we validated the trained model with an independent test set that is completely different from the training one. Furthermore, in order to assess the stability of the method we used cross-validation setting. Second, texture descriptors could be sensitive to imaging conditions such as rotations, beam angle, noise, exposure, blur, accelerating voltage, and image post-processing on digital X-ray systems. However, we tried to address this limitation by pre-processing the image data, yet the results may still be affected. Third, we selected the size and compactness parameters of the superpixel segmentation method empirically. Therefore, further investigations are required to clarify the effect of parameters used in adaptive segmentation stage. Moreover, we utilized the average mask obtained from the most informative region to reduce the computational complexity, which could lower the performance. Fourth, we believe that the performance of landmark detection algorithm has a direct effect on the analysis which is another limitation of our method. In this study, we relied on BoneFinder<sup>®37</sup> tool for landmark detection, which could be improved<sup>50</sup>. Finally, although the most informative regions we found are located at the sites where osteophytes are typically occur, we did not analyze the direct effect of the presence of osteophytes and their surrounding. More research is needed in order to assess the role of osteophytes in the SB texture, specifically within the ROIs located at bone margins.

To conclude, we believe that texture analysis methods have the potential to reveal structural changes in SB, and in particular, the association between early OA and remodeling of the fine trabecular network. This study demonstrated and confirmed that the localization of ROI plays a significant role in bone texture analysis. Our findings show that placing the ROIs at tibial margins could provide more discriminative information OA changes in the bone and lead to more sensitive imaging-based biomarkers.

## Acknowledgments

The OAI is a public-private partnership comprised of five contracts (N01-AR-2-2258; N01-AR-2-2259; N01-AR-2-2260; N01-AR-2-2261; N01-AR-2-2262) funded by the National Institutes of Health, a branch of the Department of Health and Human Services, and conducted by the OAI Study Investigators. Private funding partners include Merck Research Laboratories; Novartis Pharmaceuticals Corporation, GlaxoSmithKline; and Pfizer, Inc. Private sector funding for the OAI is managed by the Foundation for the National Institutes of Health. This manuscript was prepared using an OAI public use data set and does not necessarily reflect the opinions or views of the OAI investigators, the NIH, or the private funding partners

Multicenter Osteoarthritis Study (MOST) Funding Acknowledgment. MOST is comprised of four cooperative grants (Felson – AG18820; Torner – AG18832, Lewis – AG18947, and Nevitt – AG19069) funded by the National Institutes of Health, a branch of the Department of Health and Human Services, and conducted by MOST study investigators. This manuscript was

prepared using MOST data and does not necessarily reflect the opinions or views of MOST investigators.

We would like to acknowledge the strategic funding of the University of Oulu, Infotech Oulu.

Dr. Claudia Lindner is acknowledged for providing BoneFinder.

### Author contributions

N.B. originated the idea. N.B., A.T., and S.S. designed the study. J.H. and M.T.N. participated in conceptualization of the study. N.B. and A.T. conducted the experiments. S.S. contributed at each stage of the process and supervised the project. All authors contributed to interpreting the data, writing and editing the manuscript, and have approved the submitted version of the manuscript.

### Role of the funding source

Funding sources are not associated with the scientific contents of the study.

### Conflict of interest

The authors report no conflicts of interest.

## References

1. Buckland-Wright, C. Subchondral bone changes in hand and knee osteoarthritis detected by radiography. *Osteoarthritis and cartilage* **12**, 10–19 (2004) (on pp. 1, 2, 4, 12).
2. Kamibayashi, L., Wyss, U., Cooke, T. & Zee, B. Trabecular microstructure in the medial condyle of the proximal tibia of patients with knee osteoarthritis. *Bone* **17**, 27–35 (1995) (on pp. 1, 2).
3. Lynch, J., Hawkes, D. & Buckland-Wright, J. Analysis of texture in macroradiographs of osteoarthritic knees, using the fractal signature. *Physics in Medicine & Biology* **36**, 709 (1991) (on pp. 1, 2, 4, 12).
4. Janvier, T., Jennane, R., Toumi, H. & Lespessailles, E. Subchondral tibial bone texture predicts the incidence of radiographic knee osteoarthritis: data from the Osteoarthritis Initiative. *Osteoarthritis and cartilage* **25**, 2047–2054 (2017) (on pp. 1, 2, 4, 12).
5. Hirvasniemi, J. *et al.* Differences in tibial subchondral bone structure evaluated using plain radiographs between knees with and without cartilage damage or bone marrow lesions-the Oulu Knee Osteoarthritis study. *European radiology* **27**, 4874–4882 (2017) (on pp. 1, 2, 4, 12).
6. Ljuhar, R. *et al.* Combining fractal-and entropy-based bone texture analysis for the prediction of Osteoarthritis: data from the Multicenter Osteoarthritis study (MOST) in *RöFo-Fortschritte auf dem Gebiet der Röntgenstrahlen und der bildgebenden Verfahren* **190** (2018), WISS–106 (on pp. 1, 2, 4, 12).
7. Jennane, R., Touvier, J., Bergounioux, M. & Lespessailles, E. A variational model for trabecular bone radiograph characterization in *Biomedical Imaging (ISBI), 2014 IEEE 11th International Symposium on* (2014), 1283–1286 (on pp. 1, 2, 4, 12).
8. Kraus, V. B. *et al.* Predictive validity of radiographic trabecular bone texture in knee osteoarthritis: the Osteoarthritis Research Society International/Foundation for the National Institutes of Health Osteoarthritis Biomarkers Consortium. *Arthritis & Rheumatology* **70**, 80–87 (2018) (on pp. 1, 2, 4, 12).
9. Hirvasniemi, J. *et al.* Quantification of differences in bone texture from plain radiographs in knees with and without osteoarthritis. *Osteoarthritis and cartilage* **22**, 1724–1731 (2014) (on pp. 1, 2, 4, 12).
10. Wolski, M., Podsiadlo, P., Stachowiak, G., Lohmander, L. & Englund, M. Differences in trabecular bone texture between knees with and without radiographic osteoarthritis detected by directional fractal signature method. *Osteoarthritis and cartilage* **18**, 684–690 (2010) (on pp. 1, 2, 4, 12).
11. Thomson, J., O'Neill, T., Felson, D. & Cootes, T. Automated shape and texture analysis for detection of osteoarthritis from radiographs of the knee in *International Conference on Medical Image Computing and Computer-Assisted Intervention* (2015), 127–134 (on pp. 1, 2, 4, 12).
12. Podsiadlo, P. *et al.* Baseline trabecular bone and its relation to incident radiographic knee osteoarthritis and increase in joint space narrowing score: directional fractal signature analysis in the MOST study. *Osteoarthritis and cartilage* **24**, 1736–1744 (2016) (on pp. 1, 2, 4, 12).

13. Messent, E. A., Ward, R. J., Tonkin, C. J. & Buckland-Wright, C. Tibial cancellous bone changes in patients with knee osteoarthritis. A short-term longitudinal study using Fractal Signature Analysis. *Osteoarthritis and cartilage* **13**, 463–470 (2005) (on pp. 1, 2, 4, 12).
14. Kraus, V. B. *et al.* Trabecular morphometry by fractal signature analysis is a novel marker of osteoarthritis progression. *Arthritis & Rheumatism: Official Journal of the American College of Rheumatology* **60**, 3711–3722 (2009) (on pp. 1, 2, 4, 12).
15. Lowitz, T. *et al.* Characterization of knee osteoarthritis-related changes in trabecular bone using texture parameters at various levels of spatial resolution—a simulation study. *BoneKEy reports* **3** (2014) (on p. 1).
16. Tiulpin, A., Thevenot, J., Rahtu, E., Lehenkari, P. & Saarakkala, S. Automatic knee osteoarthritis diagnosis from plain radiographs: a deep learning-based approach. *Scientific reports* **8**, 1727 (2018) (on pp. 1, 12).
17. Neogi, T. *Clinical significance of bone changes in osteoarthritis* in *Arthritis Research & Therapy* **14** (2012), A3 (on p. 1).
18. Tiulpin, A. *et al.* Multimodal Machine Learning-based Knee Osteoarthritis Progression Prediction from Plain Radiographs and Clinical Data. *arXiv preprint arXiv:1904.06236* (2019) (on p. 1).
19. Brahim, A. *et al.* A Decision Support Tool For Early Detection of Knee OsteoArthritis using X-ray Imaging and Machine Learning: Data from the OsteoArthritis Initiative. *Computerized Medical Imaging and Graphics* (2019) (on p. 1).
20. Minciullo, L. & Cootes, T. *Fully automated shape analysis for detection of osteoarthritis from lateral knee radiographs in Pattern Recognition (ICPR), 2016 23rd International Conference on* (2016), 3787–3791 (on p. 1).
21. Antony, J., McGuinness, K., O'Connor, N. E. & Moran, K. *Quantifying radiographic knee osteoarthritis severity using deep convolutional neural networks in Pattern Recognition (ICPR), 2016 23rd International Conference on* (2016), 1195–1200 (on p. 1).
22. Hirvasniemi, J., Niinimäki, J., Thevenot, J. & Saarakkala, S. Bone Density and Texture from Minimally Post-Processed Knee Radiographs in Subjects with Knee Osteoarthritis. *Annals of biomedical engineering*, 1–10 (2019) (on p. 2).
23. Riad, R. *et al.* Texture analysis using complex wavelet decomposition for knee osteoarthritis detection: Data from the osteoarthritis initiative. *Computers & Electrical Engineering* **68**, 181–191 (2018) (on pp. 2, 4).
24. Woloszynski, T. *et al.* Prediction of progression of radiographic knee osteoarthritis using tibial trabecular bone texture. *Arthritis & Rheumatism* **64**, 688–695 (2012) (on p. 2).
25. Podsiadlo, P., Cicuttini, F. M., Wolski, M., Stachowiak, G. & Wluka, A. Trabecular bone texture detected by plain radiography is associated with an increased risk of knee replacement in patients with osteoarthritis: a 6 year prospective follow up study. *Osteoarthritis and cartilage* **22**, 71–75 (2014) (on p. 2).
26. Wolski, M., Podsiadlo, P. & Stachowiak, G. Directional fractal signature analysis of trabecular bone: evaluation of different methods to detect early osteoarthritis in knee radiographs. *Proceedings of the Institution of Mechanical Engineers, Part H: Journal of Engineering in Medicine* **223**, 211–236 (2009) (on pp. 2, 4, 12).
27. Janvier, T., Toumi, H., Harrar, K., Lespessailles, E. & Jennane, R. *ROI impact on the characterization of knee osteoarthritis using fractal analysis in Image Processing Theory, Tools and Applications (IPTA), 2015 International Conference on* (2015), 304–308 (on pp. 2, 4, 12).
28. Shamir, L. *et al.* Knee X-ray image analysis method for automated detection of Osteoarthritis. *IEEE Transactions on Biomedical Engineering* **56**, 407–415 (2009) (on pp. 2, 4).
29. Hladůvka, J. *et al.* Femoral ROIs and Entropy for Texture-based Detection of Osteoarthritis from High-Resolution Knee Radiographs. *arXiv preprint arXiv:1703.09296* (2017) (on pp. 2, 4, 12).
30. Anifah, L., Purnama, I. K. E., Hariadi, M. & Purnomo, M. H. Osteoarthritis classification using self organizing map based on gabor kernel and contrast-limited adaptive histogram equalization. *The open biomedical engineering journal* **7**, 18 (2013) (on pp. 2, 4).
31. Varma, M. & Garg, R. *Locally invariant fractal features for statistical texture classification in 2007 IEEE 11th international conference on computer vision* (2007), 1–8 (on p. 2).
32. Lynch, J., Hawkes, D. & Buckland-Wright, J. A robust and accurate method for calculating the fractal signature of texture in macroradiographs of osteoarthritic knees. *Medical Informatics* **16**, 241–251 (1991) (on p. 2).
33. Messent, E., Ward, R., Tonkin, C. & Buckland-Wright, C. Differences in trabecular structure between knees with and without osteoarthritis quantified by macro and standard radiography, respectively. *Osteoarthritis and cartilage* **14**, 1302–1305 (2006) (on p. 2).



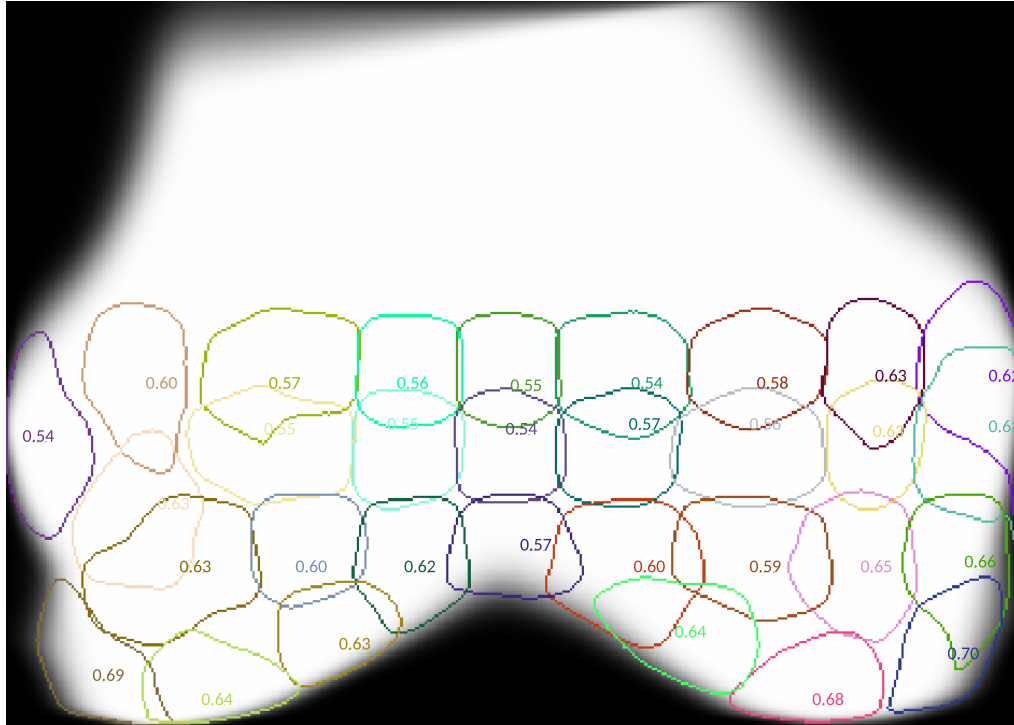
34. Woloszynski, T., Podsiadlo, P., Stachowiak, G. & Kurzynski, M. A signature dissimilarity measure for trabecular bone texture in knee radiographs. *Medical physics* **37**, 2030–2042 (2010) (on p. 2).
35. Podsiadlo, P., Wolski, M. & Stachowiak, G. Automated selection of trabecular bone regions in knee radiographs. *Medical physics* **35**, 1870–1883 (2008) (on p. 2).
36. Hafezi-Nejad, N., Guermazi, A., Demehri, S. & Roemer, F. W. New imaging modalities to predict and evaluate osteoarthritis progression. *Best Practice & Research Clinical Rheumatology* (2018) (on pp. 2, 4).
37. Lindner, C. *et al.* Fully automatic segmentation of the proximal femur using random forest regression voting. *IEEE transactions on medical imaging* **32**, 1462–1472 (2013) (on pp. 3, 12).
38. Achanta, R. *et al.* SLIC superpixels compared to state-of-the-art superpixel methods. *IEEE transactions on pattern analysis and machine intelligence* **34**, 2274–2282 (2012) (on p. 3).
39. Wolski, M. *et al.* Trabecular bone texture detected by plain radiography and variance orientation transform method is different between knees with and without cartilage defects. *Journal of Orthopaedic Research* **29**, 1161–1167 (2011) (on p. 4).
40. Shamir, L. *et al.* Early detection of radiographic knee osteoarthritis using computer-aided analysis. *Osteoarthritis and Cartilage* **17**, 1307–1312 (2009) (on p. 4).
41. Veenland, J., Grashuis, J., van der Meer, F., Beckers, A. & Gelsema, E. Estimation of fractal dimension in radiographs. *Medical physics* **23**, 585–594 (1996) (on pp. 4, 9).
42. Ojala, T., Pietikäinen, M. & Mäenpää, T. *Gray scale and rotation invariant texture classification with local binary patterns in European Conference on Computer Vision* (2000), 404–420 (on p. 7).
43. Dalal, N. & Triggs, B. *Histograms of oriented gradients for human detection in international Conference on computer vision & Pattern Recognition (CVPR'05)* **1** (2005), 886–893 (on p. 7).
44. Hirvasniemi, J. *et al.* Correlation of subchondral bone density and structure from plain radiographs with micro computed tomography ex vivo. *Annals of biomedical engineering* **44**, 1698–1709 (2016) (on p. 7).
45. Coelho, L. P. Mahotas: Open source software for scriptable computer vision. *arXiv preprint arXiv:1211.4907* (2012) (on p. 7).
46. Pedregosa, F. *et al.* Scikit-learn: Machine Learning in Python. *Journal of Machine Learning Research* **12**, 2825–2830 (2011) (on pp. 7, 8).
47. Egloff, C., Hügle, T. & Valderrabano, V. Biomechanics and pathomechanisms of osteoarthritis. *Swiss medical weekly* **142** (2012) (on pp. 9, 12).
48. Kadir, T. & Brady, M. Saliency, scale and image description. *International Journal of Computer Vision* **45**, 83–105 (2001) (on p. 9).
49. Norman, B., Pedoia, V., Noworolski, A., Link, T. M. & Majumdar, S. Applying densely connected convolutional neural networks for staging osteoarthritis severity from plain radiographs. *Journal of digital imaging* **32**, 471–477 (2019) (on p. 12).
50. Tiulpin, A., Melekhov, I. & Saarakkala, S. *KNEEL: Knee Anatomical Landmark Localization Using Hourglass Networks* 2019. arXiv: 1907.12237 [cs.CV] (on p. 12).

# Supplementary

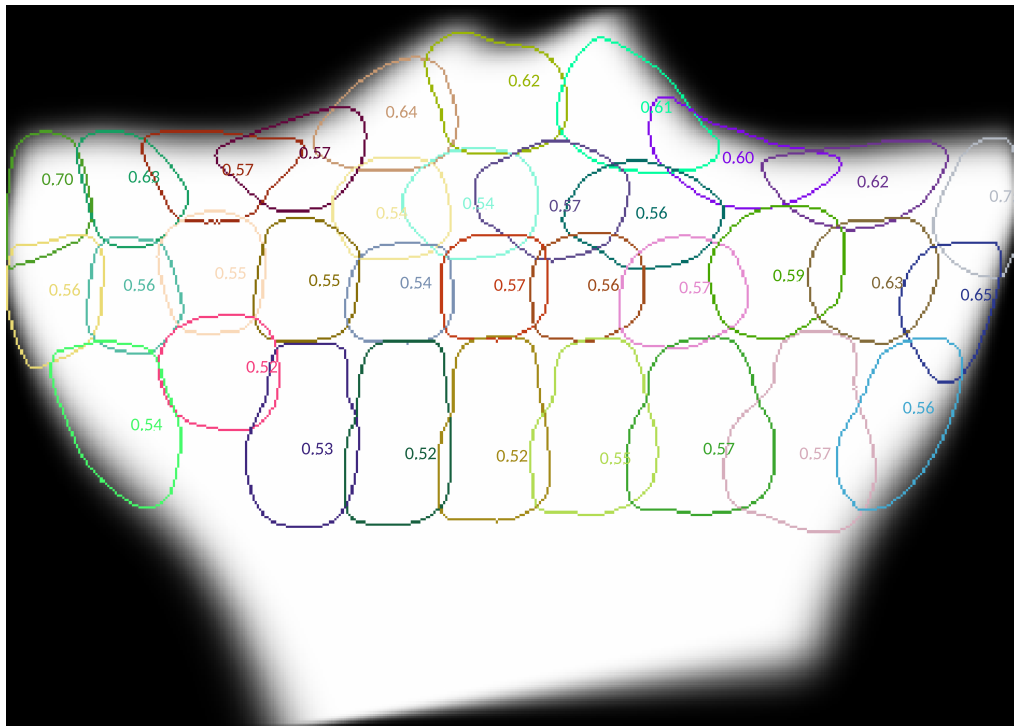
## Parameter Optimization

**Table S1.** Hyperparameter search space and best parameters found after performing grid search on 5-fold cross-validation setting.

	Hyperparameter	Type	Values	Best
LBP	Radius	Ordinal	{2,3,4,5,6}	6
	Points	Ordinal	{8,10,12,16,24}	8
HOG	Orientations	Ordinal	{4, 8, 9 ,10}	4
	Cells per block	Ordinal	{(2,2), (3, 3), (4,4), (6,6)}	4, 4
	Pixels per cell		{(6,6), (8,8), (10,10), (12,12), (14,14)}	10, 10



(a)



(b)

**Figure S1.** This figure demonstrates several adaptive regions found by our framework on (a) femur and on (b) tibia. Contours represent the thresholded mask borders. ROC AUC values based on LBP features are also shown on the figure. Some of the (overlapping) regions are excluded for illustration reasons. Best viewed on screen.

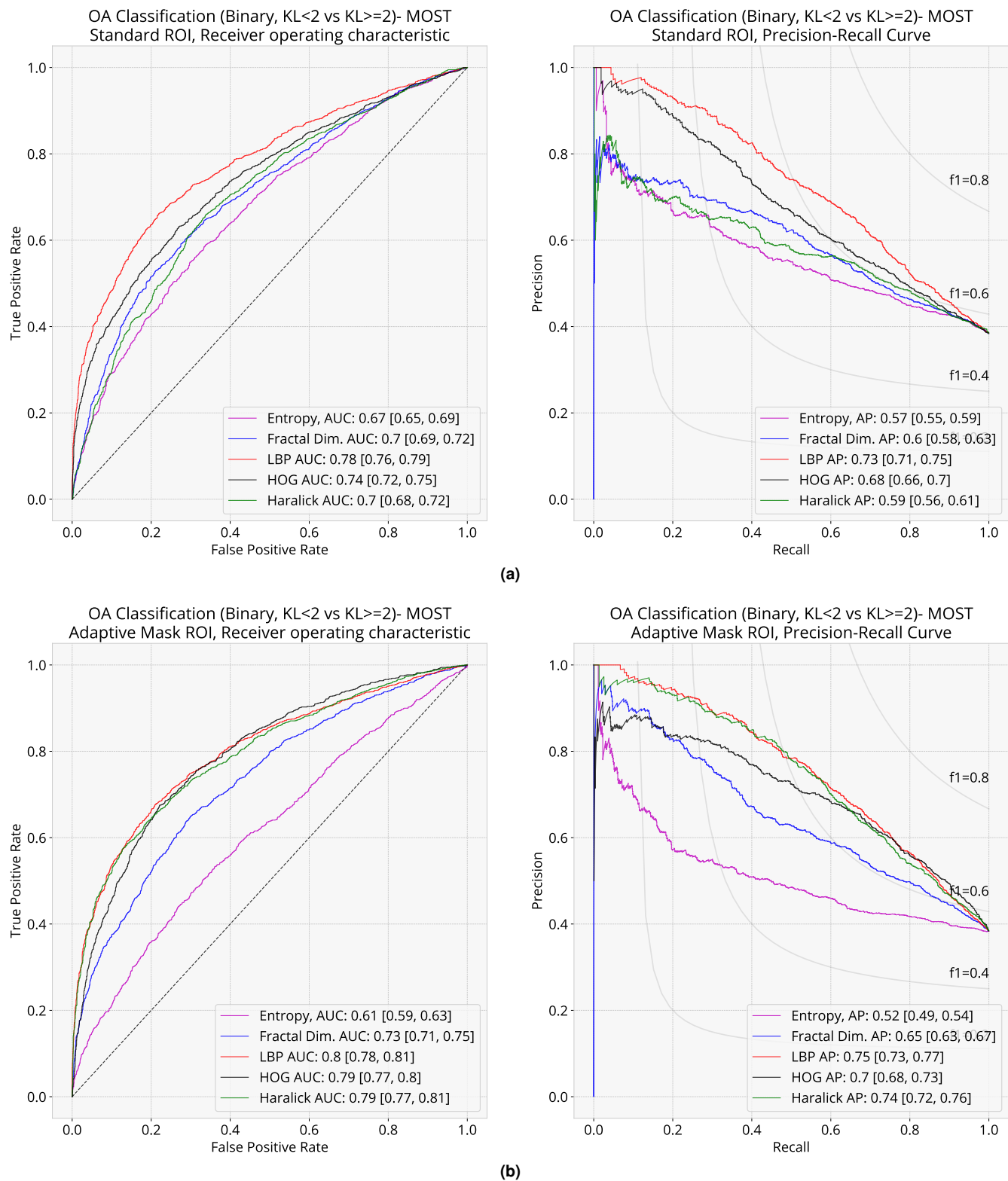


**Figure S2.** Classification performance of texture descriptors on standard ROI (a) and adaptive mask ROI (b) on **MOST** with Logistic regression on 5-fold cross validation setting. In ROC plots, labels show AUC values and the labels in PR curves show AP values with 95% confidence intervals in parentheses. Best viewed on screen.

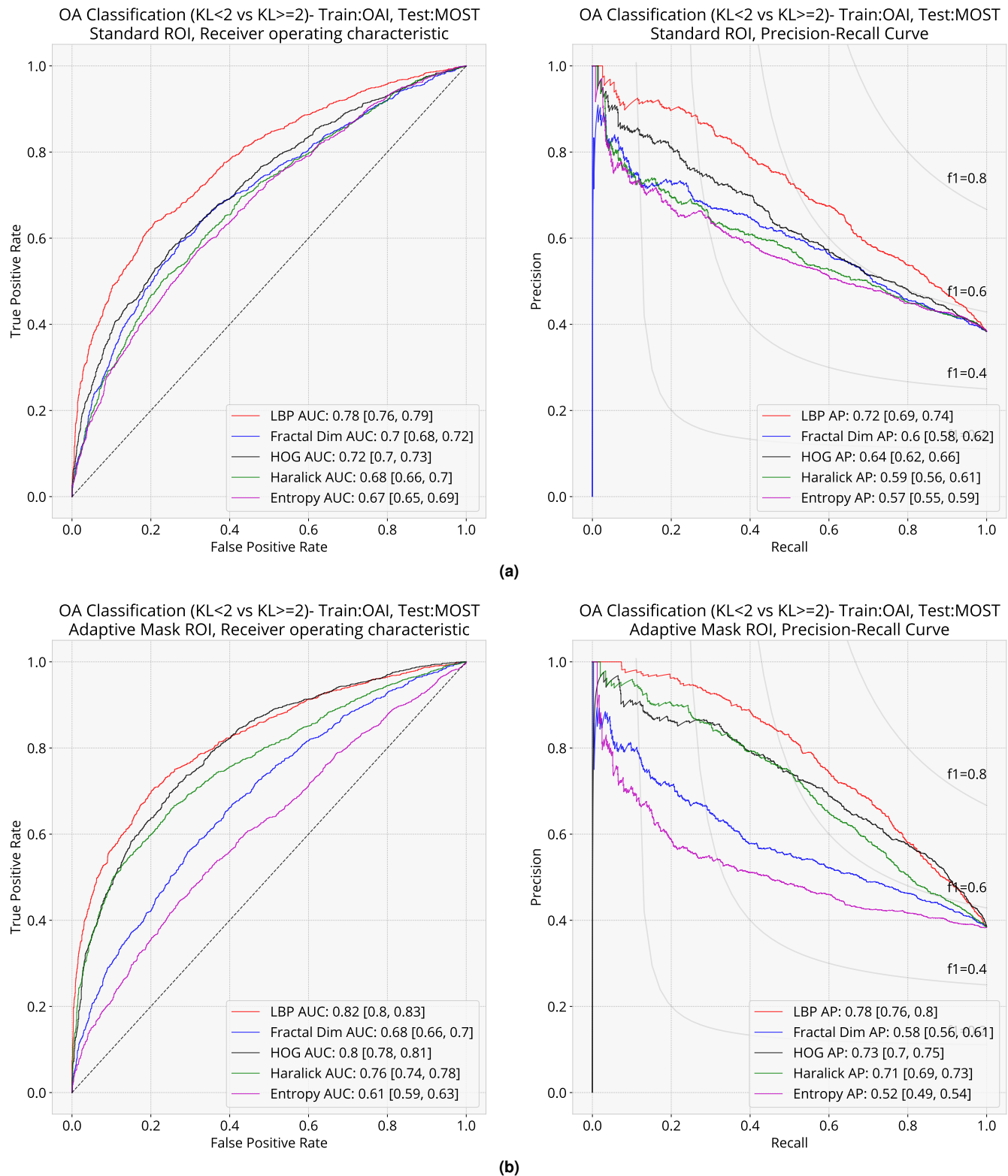


**Figure S3.** Classification performance of texture descriptors on standard ROI (a) and adaptive mask ROI (b) where we used **OAI** as the training set and **MOST** data as a test set (independent validation data). We used Logistic regression classification as before. In ROC plots, labels show AUC values and the labels in PR curves show AP values with 95% confidence intervals in parentheses. Best viewed on screen.



**Table S2.** Comparison of feature combinations computed at adaptive region **t 2.6**. Scores are given by ROC AUC and Precision-Recall AP with 95% confidence interval in parentheses.

Method	Score	OAI - Exp 1	MOST - Exp 2	Train: OAI, Test: MOST - Exp 3
LBP + HOG	AUC AP	0.767 [0.757, 0.776] 0.745 [0.733, 0.756]	0.793 [0.777, 0.808] 0.738 [0.717, 0.756]	<b>0.822 [0.808, 0.835]</b> 0.766 [0.746, 0.784]
LBP + HOG + Haralick	AUC AP	<b>0.774 [0.764, 0.783]</b> <b>0.753 [0.741, 0.764]</b>	<b>0.808 [0.793, 0.822]</b> <b>0.766 [0.747, 0.782]</b>	0.813 [0.798, 0.827] <b>0.767 [0.747, 0.785]</b>
LBP + HOG + Fractal	AUC AP	0.771 [0.760, 0.780] 0.750 [0.738, 0.761]	0.792 [0.776, 0.806] 0.739 [0.717, 0.757]	0.805 [0.790, 0.819] 0.744 [0.723, 0.765]
LBP + HOG + Fractal + Haralick	AUC AP	<b>0.774 [0.764, 0.783]</b> <b>0.754 [0.742, 0.765]</b>	0.805 [0.790, 0.819] 0.766 [0.747, 0.782]	0.802 [0.786, 0.816] 0.754 [0.733, 0.773]

**Table S3.** Combining features from adaptive region  $t_{26}$  (medial) and  $t_3$  (lateral). Scores are given by ROC AUC and Precision-Recall AP with 95% confidence interval in parentheses.

Method	Score	OAI - Exp 1	MOST - Exp 2	Train: OAI, Test: MOST - Exp 3
$LBP_{26} + LBP_3$	AUC AP	0.791 [0.782, 0.801] 0.778 [0.767, 0.788]	0.809 [0.793, 0.823] 0.769 [0.750, 0.787]	0.840 [0.825, 0.852] 0.804 [0.786, 0.820]
$HOG_{26} + HOG_{t_3}$	AUC AP	0.760 [0.749, 0.770] 0.734 [0.721, 0.745]	0.783 [0.767, 0.798] 0.691 [0.668, 0.714]	0.805 [0.789, 0.818] 0.740 [0.719, 0.758]
$FD_{26} + FD_{t_3}$	AUC AP	0.688 [0.677, 0.698] 0.646 [0.633, 0.658]	0.742 [0.725, 0.758] 0.669 [0.646, 0.690]	0.692 [0.674, 0.709] 0.588 [0.563, 0.610]
$Haralick_{26} + Haralick_{t_3}$	AUC AP	0.695 [0.684, 0.705] 0.667 [0.654, 0.680]	0.802 [0.785, 0.816] 0.767 [0.748, 0.784]	0.759 [0.741, 0.775] 0.708 [0.685, 0.729]